Title: Frictional ignition of dispersion-strengthened Ni-Cr alloys

Authors: Andres Garcia Jimenez¹, Timothy Wabel², Fabio A. Bendana³, John D. DeSain³, Michael Xu⁴, James M. LeBeau⁴, Zachary C. Cordero¹

Affiliations:

- Aeronautics and Astronautics, Massachusetts Institute of Technology, Cambridge, MA 02139
- 2. Propulsion Department, The Aerospace Corporation, El Segundo, CA 90245
- 3. Propulsion Science Department, The Aerospace Corporation, El Segundo, CA 90245
- 4. Materials Science and Engineering, Massachusetts Institute of Technology, Cambridge, MA 02139

Corresponding Author: Zachary Cordero; zcordero@mit.edu; 617.253.8821

Abstract: Frictional heating of metals at reciprocating or sliding contacts in high-pressure oxygen environments poses a risk of catastrophic metal fires. This phenomenon, known as frictional ignition, has been implicated in several high-profile failures of oxidizer-rich turbopumps, presenting an ongoing challenge in the development of next-generation reusable rocket engines. Early NASA investigations on frictional ignition of candidate turbine materials identified oxide dispersion-strengthened Ni-base superalloys as exceptionally resistant to ignition. In this study, we performed high-speed sliding, frictional ignition experiments on binary Ni-Cr alloys and two oxide dispersion-strengthened Ni-Cr alloys – MA754 and MA758. Analysis of recovered non-ignited samples revealed the in situ growth of oxide tribolayers on rubbing surfaces during sliding. An order of magnitude reduction in friction coefficient during the initial stages of sliding was attributed to the formation of these tribolayers. An abrupt increase in friction coefficient preceding ignition was linked to tribolayer breakdown, exposing the hot underlying metal to high-pressure oxygen. The oxide dispersion-strengthened alloy MA754 was the only material that did not ignite under any test conditions. Its specific content of Cr and Y₂O₃ dispersoids synergistically promote rapid growth of a thick, adherent oxide tribolayer strengthened by refractory Ni₂CrO₄ precipitates. These features collectively mitigate tribolayer breakdown, suppressing ignition. The findings highlight the critical role of tribolayer stability in achieving frictional ignition resistance and suggest alloy design strategies for tailoring oxidational wear behaviors to develop intrinsically ignition-resistant materials.

Keywords: tribochemistry, alloy design, oxidation, sliding wear, metal combustion

1. Introduction

The oxidizer-rich turbopumps in oxidizer-rich staged combustion and full-flow staged combustion rocket engines subject the turbine to a high-temperature, high-pressure oxygen-rich environment. Under these conditions, rubbing of the rotor against stationary components can result in frictional ignition, a catastrophic failure mode [1]. There are two main approaches to mitigate frictional ignition. One is to increase clearances around the rotor. However, this approach sacrifices efficiency which must be compensated by increasing the turbine inlet temperature, potentially degrading service life and exacerbating other ignition mechanisms. The second, preferred approach is to use intrinsically ignition-resistant materials at locations where

rubs are expected. Such materials can be applied as coatings or in bulk form, and are either intrinsically inert or exhibit favorable oxidation behaviors.

Historically, selection of ignition-resistant materials for oxygen-rich turbines has relied on test data collected by NASA White Sands Testing Facility (WSTF) [1–5]. In the WSTF studies, a specialized rub rig was used to investigate frictional ignition in a high-pressure O₂ environment. A wide range of different alloys were assessed, and their ignition behaviors were found to depend strongly on composition. Ferrous alloys and Ni-base alloys with high Fe content ignited more readily than low-Fe Ni-base alloys [2,5]. An oxide tribolayer was observed on non-ignited specimens recovered from interrupted tests. This tribolayer protected against further oxidation and lubricated the sliding surface, decreasing the friction coefficient [1–3,5]. Onset of frictional ignition was speculatively linked to breakdown of the tribolayer, which exposed the underlying hot metal to high-pressure O₂, triggering a metal fire [1,2,4,5].

A key finding from the WSTF work was that MA754, an oxide dispersion-strengthened superalloy, possessed exceptional ignition resistance [2]. *In situ* measurements of the friction coefficient and qualitative post-mortem observations of recovered MA754 specimens indicated that its ignition resistance stems from the growth of an extremely robust oxide tribolayer [2]. While there is limited work on oxidational wear of MA754, especially during high-speed sliding under high oxygen pressures, the static oxidation behavior of MA754 has been thoroughly investigated. Under static conditions, MA754 exhibits slow oxide growth because of its high Cr content, which promotes the rapid formation of a continuous protective Cr₂O₃ overlayer. Y₂O₃ dispersoids further enhance oxidation resistance by inhibiting short-circuit along grain boundaries [6–9] and by improving oxide adhesion via growth of oxide pegs and elimination of porosity at the metal/oxide interface [10,11]. Because of complicating tribological effects during sliding contact these phenomena may not directly translate to oxide tribolayer growth, motivating the present study.

Here we assess the effects of Cr content and Y₂O₃ dispersoids on frictional ignition resistance through frictional ignition experiments on binary Ni-Cr alloys and the ODS Ni-Cr alloys MA754 and MA758. We combine our experimental results with finite element simulations of frictional heating to determine ignition temperatures. We also characterize the rubbing surfaces on recovered samples, focusing specifically on the oxide tribolayer, and compare our findings with past observations from high-speed sliding tests and static oxidation experiments. These results reveal the unique features of the MA754 tribolayer that contribute to its ignition resistance, suggesting guidelines for designing and selecting ignition-resistant materials.

2. Methods

2.1. Frictional ignition experiments

Fictional ignition experiments were performed using a specialized rig depicted in **Figure 1**. A detailed description of this setup is given in [12,13]. During testing, a pair of identical cylindrical specimens (height = 2.54 cm, outer diameter = 2.54 cm, wall thickness = 2.54 mm) were rubbed against the flat mating surface highlighted in **Figure 1**. One sample (stator) was held fixed. The other (rotor) was attached to a shaft driven by an induction motor. The axial deformation of the specimens was measured with 10 nm accuracy using a laser displacement sensor. Frictional

forces at the rubbing interface were measured using the torque-producing current output from the motor, accounting for losses at the labyrinth seals. The specimens were imaged *in situ* through a viewport using a high-speed camera with a 10 kHz frame rate. Ignition was detected by rapid excursions in axial displacement or gas pressure.

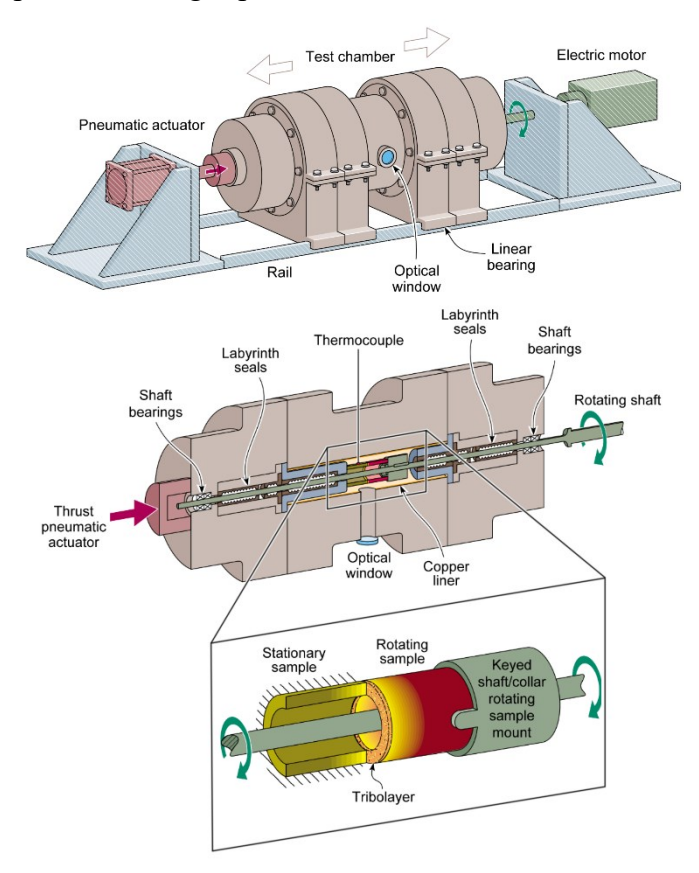


Figure 1: Frictional ignition rig: external view and cross-sectional view, with magnified inset of test specimens and rubbing surface.

Tests were run on binary Ni-Cr alloys as well as two ODS alloys – MA754 (Ni-20Cr-0.3Al-1.0Fe-0.5Ti-0.6Y₂O₃, wt%) and MA758 (Ni-30Cr-Al-1.0Fe-0.5Ti-0.6Y₂O₃, wt%). The nominal purities of Ni and the Ni-Cr alloys were 99.6% and 99.9%. **Figure 2** shows the room-temperature thermal conductivity (κ), room-temperature yield strength (σ_y), and solidus temperature (T_m) of these materials. Prior to testing, the specimens were cleaned following ASTM G93-03 [14]. Ignition behaviors were assessed in dry O₂ under gas pressures of 3.4 and 6.9 MPa. All tests used a shaft speed of 17000 rpm, corresponding to a linear sliding speed (ν) of 22 m/s. The contact load (L) was ramped linearly with time at 31 N/s, corresponding to 101 kPa/s. At the end of each test, the samples were immediately separated, rotation was stopped, and the test chamber was purged with N₂.

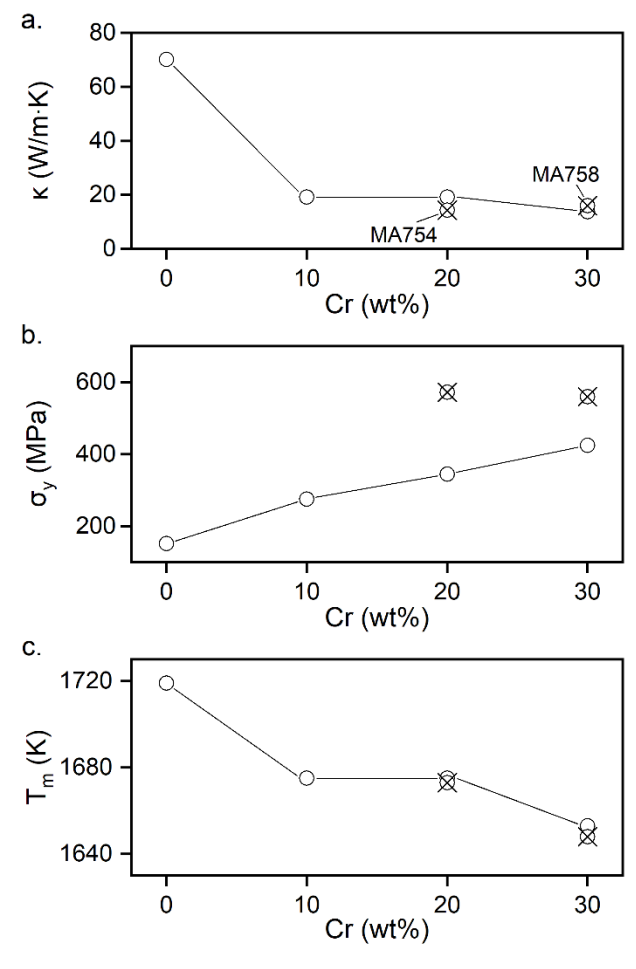


Figure 2: (a) Room-temperature thermal conductivity (κ), (b) room-temperature yield strength (σ_y), (c) solidus temperature (T_m) of the different materials.

2.2. Tribolayer characterization

Recovered specimens were inspected visually and with optical and electron microscopy. X-ray diffraction using a Co X-ray source was used to determine the phases at the rubbing interface. Non-ignited samples were mounted, cross-sectioned, mechanically polished, and imaged using a scanning electron microscope (SEM) equipped with energy dispersive X-ray spectroscopy (EDS). The hardness near the rubbing interface was characterized using nanoindentation with a diamond Berkovich tip under a fixed maximum load of 10 mN.

The rubbing surface of MA754 was imaged using scanning transmission electron microscopy (STEM). STEM lamella specimens were prepared using the FIB liftout technique. Decreasing ion beam energies of 30 kV, 16 kV, and 5 kV were used to thin the lamella. Final milling was performed at energies of 0.3 kV and 0.1 kV using an Ar ion mill to remove any Ga ion damage. STEM images were acquired with a probe-corrected Thermo Fisher Scientific Themis Z S/TEM using a probe convergence semi-angle of 18.8 mrad. STEM EDS was performed using a Thermo Fisher Scientific Super X detector using a beam current of 200 pA and processed using the Thermo Fisher Scientific Velox software.

2.3. Computational modeling

Experimental measurements of friction coefficient and contact load were used in finite element simulations to compute the interfacial temperature at the rubbing surface. The simulations were carried out using COMSOL Multiphysics® software [15]. The simulations are described at length in [16]. The thermal conductivity and volumetric heat capacity of the alloys and O₂ gas were functions of temperature. Temperature-dependent properties were obtained from the open literature [17–20] and linearly extrapolated for temperatures outside the available range.

The simulation domain was assigned an initial temperature of 298 K. Frictional heating was modeled as a heat flux boundary condition (q) at the rubbing interface:

$$q = \alpha \mu P \omega r \tag{1}$$

where ω is angular speed (1780 rad/s), r is radial distance, P is contact pressure, and α is the heat partition coefficient. Heat flux from the frictional heating was equally divided between the rotor and stator, i.e., $\alpha = 0.5$. The time-dependent friction coefficient μ was calculated using

$$\mu = ae^{-\frac{t}{\tau}} + \mu_{ss},\tag{2}$$

where a and τ are material-dependent constants, and μ_{ss} is the steady-state friction coefficient. This function was fitted to the experimental friction coefficient data of each material. The simulations did not include enthalpy of oxidation because its effect on interfacial heating is negligible prior to ignition. The side surfaces of the simulation domain (i.e., the inner walls of the pressure vessel) were assigned fixed temperature boundary conditions (T = 298 K) because of the large thermal mass of the MK500 pressure vessel.

Thermochemical calculations of alloy oxidation were carried out using the FactSage software with FTOxid, FactPS, and FSsteel databases [21]. These calculations were used to corroborate the EDS and X-ray measurements, providing additional insight into phase equilibria at the rubbing interface.

3. Experimental results and discussion

3.1. Summary of frictional ignition behaviors

Figure 3 shows representative time-series images of a frictional ignition event during a test on Ni-20Cr. At t = 51 s the first signs of ignition were observed – sparks, molten metal, and oxide slag are ejected from the rubbing surface. After an additional 80 ms, ignition was detected through a spike in chamber pressure. Finally, after 160 ms, the test was shut down and the chamber purged with N_2 . The other materials exhibited similar ignition behaviors.

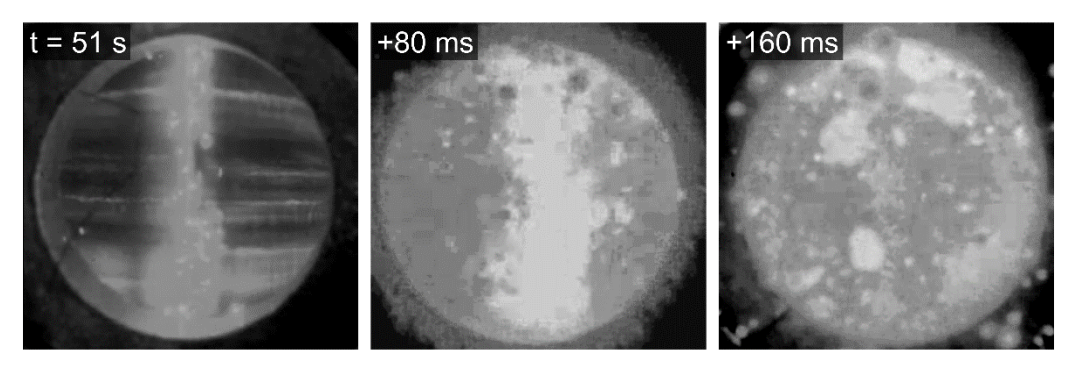


Figure 3: *In situ* time-series images of a Ni-20Cr frictional ignition event. Test conditions: v = 22 m/s, L = 31 N/s, $PO_2 = 3.4$ MPa.

Table 1 summarizes results from the frictional ignition experiments under the two different oxygen pressures. Under $PO_2 = 3.4$ MPa, all materials ignited except MA754. Among materials that ignited, ignition times (t_s) were all similar, ranging from a minimum of 43 s for Ni-30Cr to a maximum of 51 s for Ni-20Cr. Under $PO_2 = 6.9$ MPa, all materials ignited except Ni and MA754. The Ni test terminated after 53 s because of excessive specimen deformation, while the MA754 test ran for 120 s. Ignition times under the higher PO_2 were roughly twice those observed under $PO_2 = 3.4$ MPa. This ignition delay with increasing PO_2 results from an increase in gas thermal conductivity, which helps remove heat from the rubbing surface. The maximum contact pressures (σ_{max}) in these different tests ranged from 8 to 23 MPa, the maximum contact pressure achievable with the actuator and specimen geometry.

Table 1: Results from frictional ignition tests with sliding speed v = 22 m/s and loading rate L = 31 N/s.

Alloy	$PO_2 = 3.4 \text{ MPa}$					$PO_2 = 6.9 \text{ MPa}$			
	$t_{s}\left(s\right)$	$\sigma_{max}\left(MPa\right)$	μ_{ss}	$T_{p}(K)$	$t_{s}\left(s\right)$	$\sigma_{max}\left(MPa\right)$	μ_{ss}	$T_{p}(K)$	
Ni	44	8.8	0.094	1080	53 [‡]	10.8↓	0.099^{1}	1380 [‡]	
Ni-10Cr	48	9.8	0.051	1380	72	14.3	0.056	1580	
Ni-20Cr	51	11.1	0.046	1420	118	22.8	0.028	1630	
Inconel MA754	120 [‡]	23.6^{1}	0.023^{\downarrow}	1540 [‡]	120 [‡]	23.0^{1}	0.028^{1}	1490 [‡]	
Ni-30Cr	43	8.6	0.047	1300	65	14.2	0.040	1470	
Inconel MA758	44	8.9	0.040	1260	91	18.1	0.035	1430	

[‡]Ignition was not detected

Figure 4 shows ignition time as a function of Cr content. For non-ODS materials, ignition time is longest for Ni-20Cr under both PO₂ test conditions. Comparing MA754 and MA758 with their non-ODS counterparts shows that Y_2O_3 additions improve ignition resistance, though the benefit depends on PO₂ and Cr content. Under PO₂ = 3.4 MPa, MA758 has the same ignition time as Ni-30Cr whereas under PO₂ = 6.9 MPa the ignition time of MA758 is delayed 25 s. The benefit of Y_2O_3 additions is even more significant in MA754, highlighting a synergistic effect between 20 wt% Cr content and Y_2O_3 .

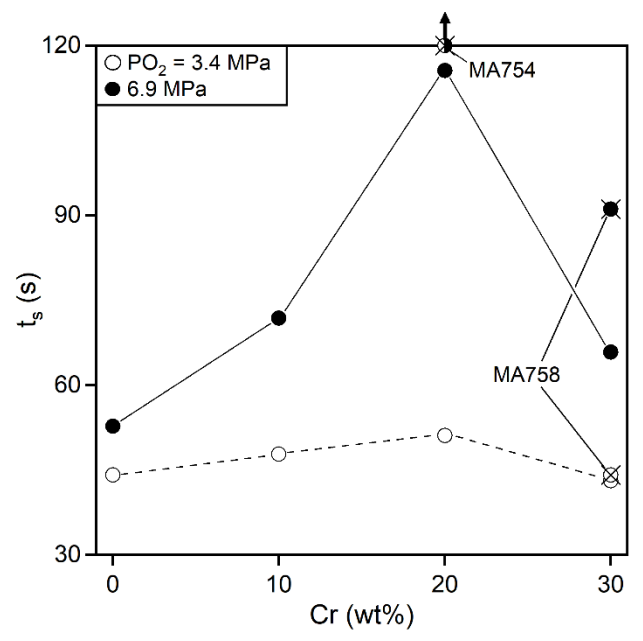


Figure 4: Test duration plotted against Cr content. All tests resulted in specimen ignition, except for Ni under $PO_2 = 6.9$ MPa and MA754 under both pressures. Vertical arrow indicates runout of the MA754 experiments.

3.2. Trends in friction coefficient

Figure 5 shows the friction coefficient as a function of time for several exemplary tests. The time evolution of the friction coefficients follows a similar form for all materials: at first contact the friction coefficient ranges between 0.1-0.3, typical of low-speed sliding contact between metals, then it decays with time to a lower steady-state value which depends on material chemistry. The time constant of this exponential decay increases with Cr content, from 10 s for Ni to 35 s for Ni-20Cr. The form and magnitude of these friction coefficient curves were insensitive to PO_2 . There are large random fluctuations at the beginning of the test that may result from specimen misalignment or running-in. Smaller periodic fluctuations with a frequency of $\sim 2 \text{ s}^{-1}$ are evident at later times in select curves.

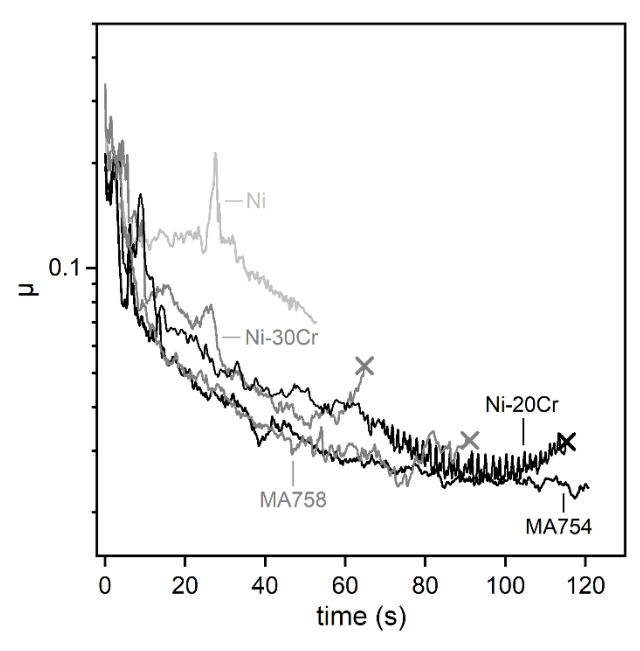


Figure 5: Friction coefficient as a function of time under $PO_2 = 6.9$ MPa. Crosses indicate ignition. The Ni test terminated early because of excessive specimen deformation.

These friction coefficient measurements are broadly consistent with data available in the open literature. Our steady-state friction coefficients for Ni and MA754 match those reported by NASA [2]. The decrease in friction coefficient seen in **Figure 5** aligns with earlier NASA WSTF reports [1–3] and with previous work on high-speed oxidational wear of steels [22–27]. In a series of high-speed sliding studies, Cocks explicitly linked low steady-state friction coefficients to growth of an oxide tribolayer through post-mortem characterization of recovered specimens and by cycling the test atmosphere between argon and air [23,24]. We thus ascribe the drop in friction coefficient in **Figure 5** with formation of a lubricating oxide tribolayer. For materials that ignited, the friction coefficient began to increase at the end of the test. We hypothesize that the rise in friction coefficient prior to ignition results from oxide tribolayer breakdown, exposure of the underlying metal, and formation of metallurgical junctions. The unprotected hot metal then reacts with high-pressure oxygen resulting in metal ignition.

Figure 6 shows the time-averaged steady-state friction coefficient μ_{ss} as a function of Cr content. Among the non-ODS materials, the friction coefficient decreases with Cr content to a minimum of 0.03 under 6.9 MPa for Ni-20Cr. A similar effect has been observed in low-speed, high-temperature sliding experiments on binary Ni-Cr alloys [25]. MA754 and MA758 have slightly lower friction coefficients than Ni-20Cr and Ni-30Cr, suggesting another benefit of Y₂O₃ addition in high-speed sliding.

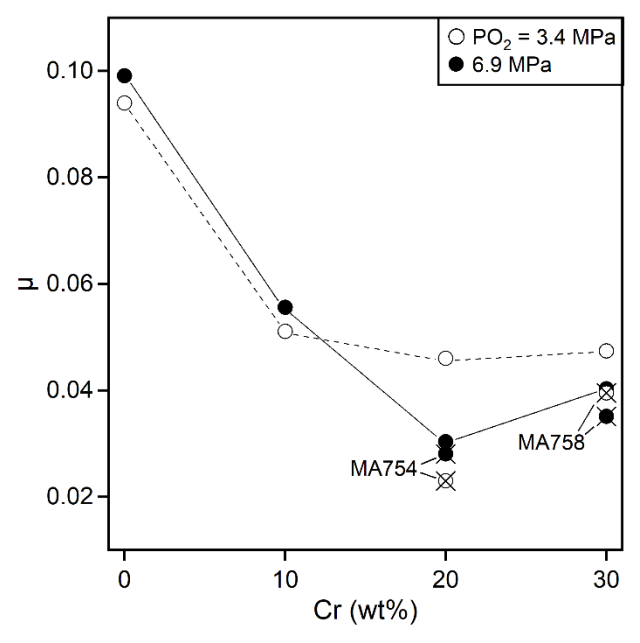


Figure 6: Time-averaged steady-state friction coefficient as a function of Cr content.

3.3. Trends in ignition temperature

Figure 7 shows interfacial temperature as a function of time under $PO_2 = 6.9$ MPa, calculated using finite element analysis with smoothed friction coefficient data from Figure 5. All the temperature-time curves have a similar form: the temperature increases rapidly over the first 10 s due to the initially high friction coefficient, then the heating rate slows as the friction coefficient decays and heat diffuses away from the rubbing surface. MA754 and MA758 exhibit an anomalously slow heating rate after their friction coefficients decay to a low steady-state value.

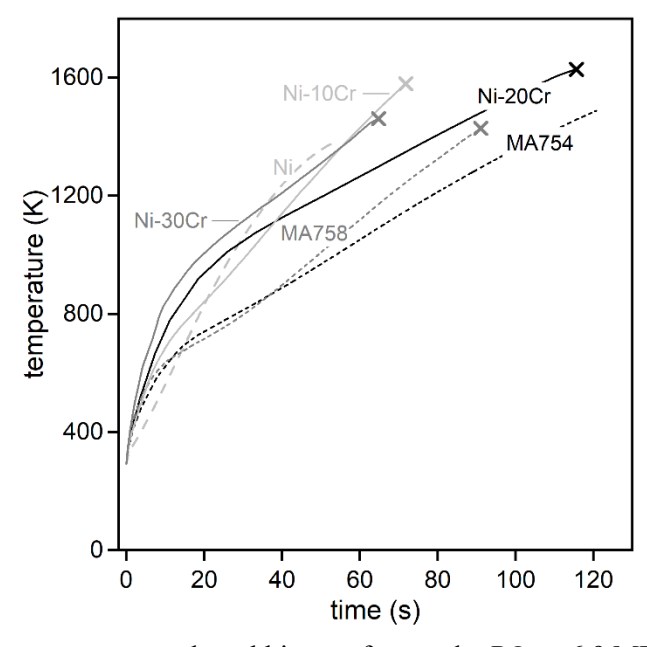


Figure 7: Interfacial temperature at the rubbing surface under $PO_2 = 6.9$ MPa as a function of time. Crosses indicate ignition.

Peak interfacial temperatures (T_p) are plotted against Cr content in **Figure 8**. These peak temperatures correspond to ignition temperatures, except for Ni under PO₂ = 6.9 MPa and MA754 under both pressures, since these specimens did not ignite. Comparing ignition temperatures under the two different pressures shows that lowering the pressure decreased the ignition temperature by 100–250 K across the full range of compositions. These ignition temperatures correspond to homologous temperatures of 0.87–0.97 under PO₂ = 6.9 and 0.73–0.85 under PO₂ = 3.4 MPa. Among non-ODS alloys, Ni-20Cr has the highest ignition temperature under all test conditions.

The effect of Y₂O₃ on ignition temperature depends on Cr content. In the MA758/Ni-30Cr material couple, Y₂O₃ has a marginal effect on ignition temperature. By contrast, in the MA754/Ni-20Cr couple, Y₂O₃ increases the ignition temperature under low PO₂, since the peak interfacial temperature in the MA754 test exceeds the ignition temperature of Ni-20Cr by 100 K. Under high PO₂, the MA754 and Ni-20Cr experiments ran for similar times, but the peak interfacial temperature in the MA754 test never reached the ignition temperature of Ni-20Cr because of the low steady-state friction coefficient of MA754.

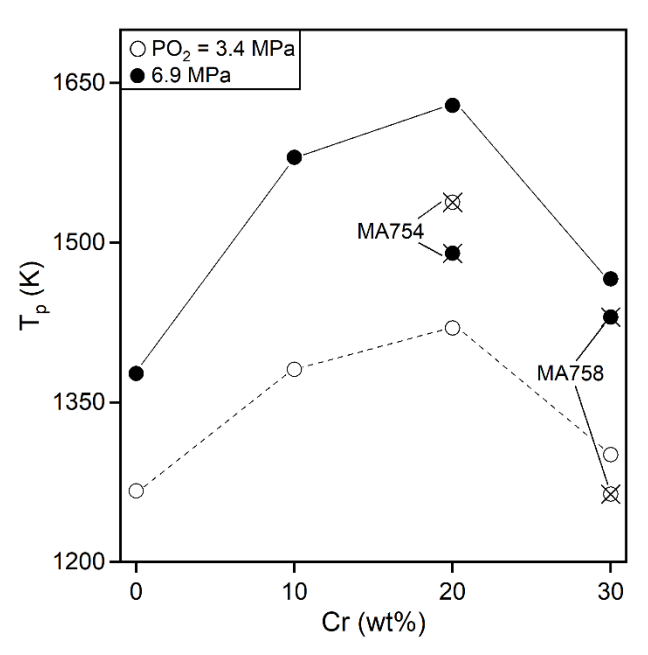


Figure 8: Peak interfacial temperature as a function of Cr content.

A possible explanation for the discrepancy between the ignition temperatures under different PO_2 is localized flash heating at asperity contacts, which causes the local temperature at ignition to be the same under both pressures. Flash heating has been studied extensively in the context of wear, and Lim and Ashby [28] have developed a flash heating model for pin-on-disk contacts. Here we extend their model to our experimental setup by modifying the expressions for the number of asperities N and normalized sliding velocity $\tilde{\mathbf{v}}$ to account for our specimen geometry [28]. The modified flash heating expression is

$$T_f = T_b + \frac{\sqrt{\pi} \mu \omega}{6 \kappa} \sqrt{\frac{PH}{N(r_o^2 - r_i^2)}} (r_o^3 - r_i^3), \tag{3}$$

where T_b is the bulk interfacial temperature computed from the finite element simulations, μ is the friction coefficient, ω is the angular velocity, κ is the thermal conductivity of the material, P is the contact pressure, and r_o and r_i are the outer and inner radii of the sample. H is the temperature-dependent hardness obtained from tabulated data in the literature [29] and interpolated over the full temperature range. N is the number of contact asperities, given by

$$N = \frac{r_o^2 - r_i^2}{r_o^2} \left(1 - \frac{P}{H} \right) \frac{P}{H} + 1, \tag{4}$$

where r_a is the average asperity radius. The following calculations used the experimentally determined asperity radius of 1 μ m. However, r_a has only a weak effect on the flash temperature at ignition: under PO₂ of 6.9 MPa, the ignition temperature of Ni-20Cr is 1630 K with r_a = 1 μ m v. 1660 K with r_a = 10 μ m.

The results of the flash heating calculation for Ni-20Cr are shown in **Figure 9**. Under both pressures, the flash heating increment over the bulk temperature decreases from \sim 400 K to 20 K over the course of the experiment as the number of asperities decreases and the mean asperity radius increases. After accounting for flash heating effects, the final interfacial temperature of 1430 K under $PO_2 = 3.4$ MPa is still 200 K below the ignition temperature under $PO_2 = 6.9$ MPa. Clearly flash heating alone cannot explain the lower ignition temperatures observed under $PO_2 = 3.4$ MPa.

The drop in ignition temperature may instead reflect a transition in the dominant ignition mechanism. Under $PO_2 = 6.9$ MPa, ignition temperatures approach the melting point of each alloy suggesting that *melting* drives tribolayer breakdown and subsequent ignition. Under $PO_2 = 3.4$ MPa, ignition occurs at significantly lower temperatures and shorter times, suggesting a *thermo-mechanical mechanism* drives ignition. This transition in ignition mechanism with PO_2 may result from slower oxidation kinetics under low PO_2 , leading to the growth of a thinner, less adherent oxide tribolayer that is more susceptible to mechanical breakdown.

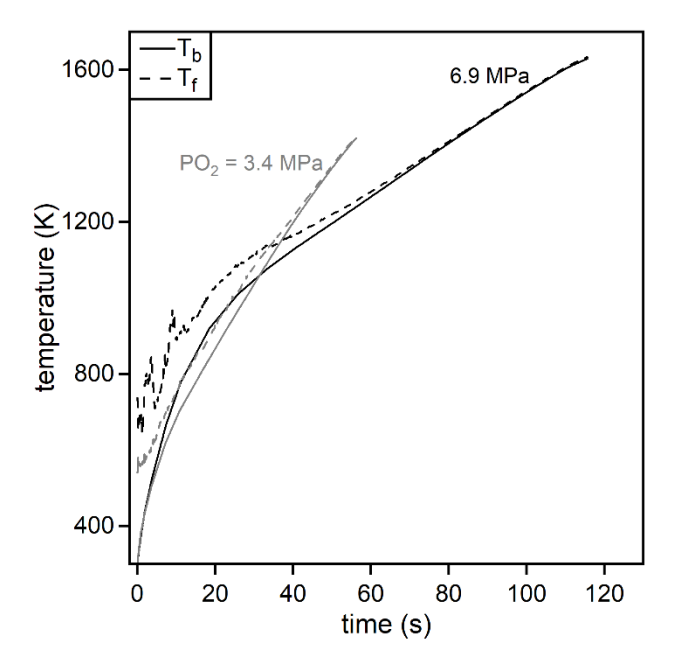


Figure 9: Flash temperature T_f and bulk interfacial temperature T_b at the rubbing surface as a function of time for Ni-20Cr under the two different O_2 pressures.

3.4. Trends in axial displacement

Axial displacement data from select tests is shown in **Figure 10**. All materials except MA758 exhibited a brief initial period of thermal expansion followed by compressive plastic deformation as a result of thermal softening under the increasing contact load. MA758 exhibited initial gradual thermal expansion which plateaued towards the end of the test. Comparing the axial displacement data shows that Cr addition imparted high-temperature strength which suppressed plastic deformation.

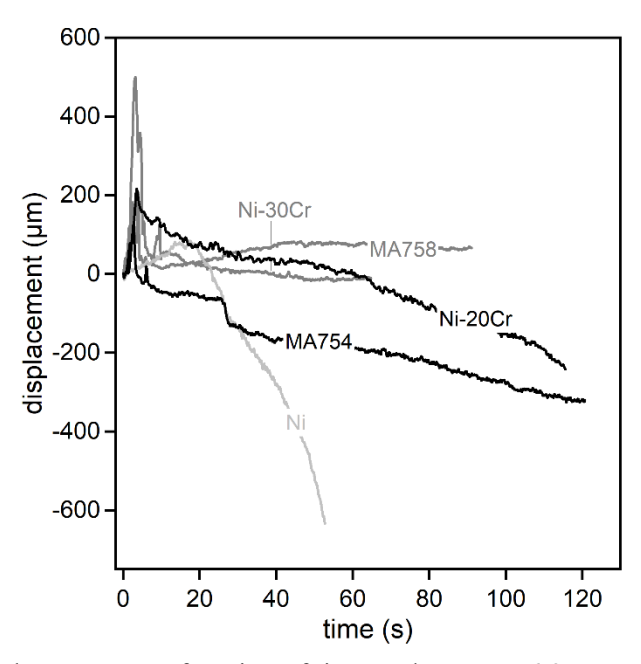


Figure 10: Axial displacement as a function of time under $PO_2 = 6.9$ MPa.

Figure 11 compares recovered Ni, Ni-20Cr, and MA754 test specimens to highlight their different deformation behaviors. All recovered materials, including those not shown in Figure 11, exhibited plastic deformation near the rubbing surface where material was extruded outward. Recovered samples also featured discoloration near the rubbing surface because of high-temperature oxidation. Comparing the Ni specimen with the Ni-20Cr specimen, which ran twice as long, achieved a ~ 100 K higher interfacial temperature, and experienced a 12 MPa higher contact stress, shows how Cr addition suppresses plastic deformation. Comparing the Ni-20Cr and MA754 specimens, which both ran for ~ 120 s, highlights how Y_2O_3 further reduces the extent of plastic deformation via dispersion-strengthening.

The rubbing surface of all recovered specimens featured an oxide tribolayer that formed *in situ*. Similar oxide tribolayers were observed by Cocks [23,24] and Stoltzfus et al. [1,2] in their studies on dry high-speed sliding contact of metals.

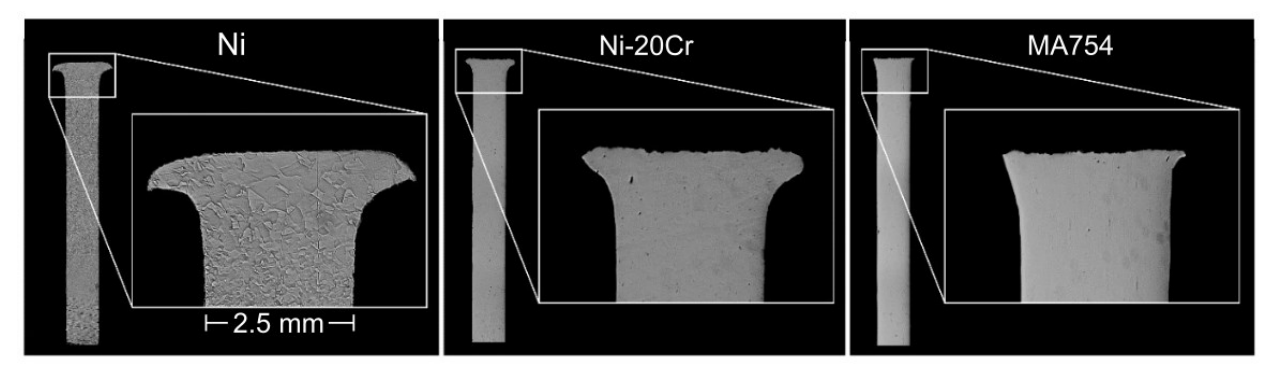


Figure 11: Macrographs of non-ignited samples. Test duration (t_s), interfacial temperature (T_p), and contact pressure (σ_{max}) at test termination for the different samples are as follows: Ni (t_s = 53 s, T_p = 1380 K, σ_{max} = 11 MPa), Ni-20Cr (117 s, 1470 K, 23 MPa), MA754 (121 s, 1490 K, 23 MPa).

4. Quantification of frictional ignition resistance

In the frictional ignition work by NASA WSTF, the product of sliding speed v and contact pressure P at ignition were used to rank the relative ignition resistance of different materials [8]. While a material with a higher Pv product will take longer to ignite under one set of conditions, the Pv product can vary strongly with O_2 partial pressure and ambient temperature, limiting its usefulness when selecting materials for operating conditions outside those tested [8]. A more general approach for assessing frictional ignition resistance is with a material index, i.e., a grouping of material properties whose extremal value maximizes performance. In **Appendix 1** we develop the following material index for frictional ignition resistance:

$$MI = \left[\frac{1}{\mu} \left(T_{ign} - T_0\right) \sqrt{\rho C_p \kappa}\right]^2,\tag{5}$$

where $\sqrt{\rho C_p \kappa}$ is the thermal effusivity, μ is the friction coefficient, T_0 is the initial specimen temperature (298 K), and T_{ign} is a material-specific ignition temperature. This material index is directly proportional to ignition time, meaning materials with a high MI will take longer to ignite. The material index is maximized by a high ignition temperature, high thermal effusivity, and low friction coefficient.

Figure 12 uses this material index to compare the frictional ignition resistance of the alloys tested here against other results from the open literature [1,2,16]. Because MA754 did not ignite under any test conditions, its ignition temperature is assumed to equal its solidus temperature. The dashed lines in Figure 12 indicate material index iso-contours. Ignition resistance increases moving towards the bottom-right corner of Figure 12. Ferrous alloys and alloys with high Fe concentrations (e.g., IN718, IN706) are the least ignition-resistant, consistent with their extreme flammability in promoted combustion testing [30,31]. Ni-base alloys with low Fe content, such as the materials in the present study, are the most ignition-resistant. The high friction coefficient of Ni makes it the least ignition resistant of the materials tested here. At the opposite extreme, the low friction coefficient and high ignition temperature of MA754 results in exceptional ignition resistance, outperforming other alloys commonly used in high pressure O₂ environments.

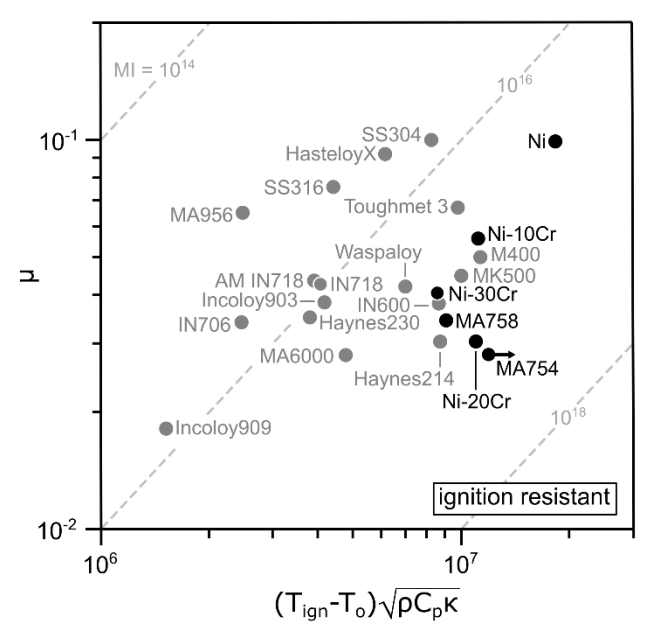


Figure 12: Frictional ignition property diagram with $T_0 = 298$ K. Data points in black correspond to alloys tested in this work.

In the following sections, we characterize the rubbing surfaces of recovered specimens, focusing specifically on the oxide tribolayer that forms *in situ*, to link the trends in friction coefficient and ignition temperature highlighted in **Figure 12** with microstructural features.

5. Structural characterization of oxide tribolayers

5.1. Overview of structure at the sliding interface

Inspection of the rubbing surfaces on all non-ignited samples revealed wear marks aligned with the sliding direction and thin interconnected mud cracks, as shown in **Figure 13**. The rubbing surfaces of the Ni-20Cr and MA754 specimens also featured periodic radial cracks with a mean spacing of \sim 150 μ m. These periodic cracks likely resulted from tensile hoop stresses caused by the thermal expansion mismatch between the oxide tribolayer and metal substrate. In select specimens, fragments of the oxide tribolayer spalled due to buckling delamination from compressive stresses that developed during rapid cooling following test shutdown.

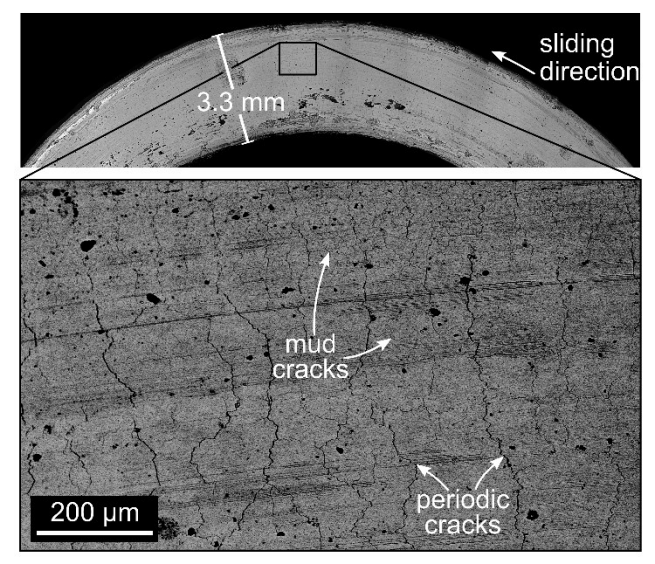


Figure 13: SEM micrographs of the rubbing surface on a non-ignited Ni-20Cr sample. Test conditions were $PO_2 = 6.9$ MPa, v = 22 m/s, L = 31 N/s. Test duration was 117 s and the peak interfacial temperature was 1470 K.

Cross-sections of the rubbing surfaces of non-ignited samples are shown in **Figure 14**. The Ni-Cr alloys developed a thicker, less porous oxide tribolayer compared to Ni. MA754 and Ni-20Cr have the thickest tribolayers, reflecting the longer test times and higher interfacial temperatures. While Ni-20Cr and MA754 ran for similar times and reached comparable interfacial temperatures, the tribolayer on MA754 is substantially thicker and less porous than the tribolayer on Ni-20Cr, suggesting Y_2O_3 accelerates oxide growth under high-speed sliding conditions. These features – thicker and less porous tribolayer – are not directly translated to Ni-30Cr, as the addition of Y_2O_3 led to a thinner tribolayer in MA758.

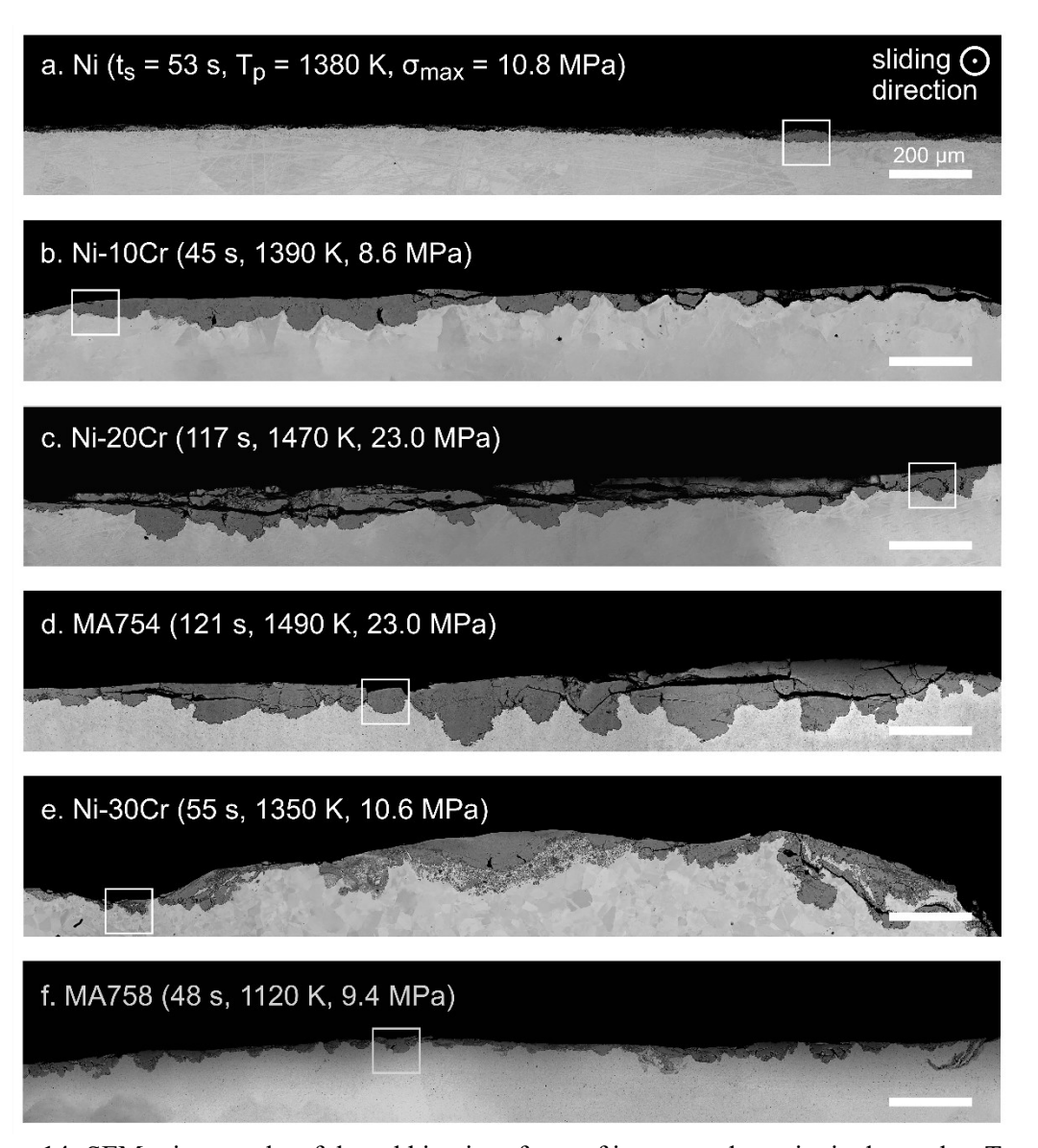


Figure 14: SEM micrographs of the rubbing interfaces of interrupted non-ignited samples. Test conditions: $PO_2 = 6.9$ MPa, v = 22 m/s, L = 31 N/s. **Figures 15** and **18** are high-magnification views of the boxed regions in these micrographs.

All samples show signs of extensive plastic deformation near the rubbing surface. In the Ni and MA754 specimens, there are fine grained regions below the metal/oxide interface which formed through dynamic recrystallization. In the MA758 and Ni-30Cr specimens, there is mechanical mixing of the tribolayer and underlying metal due to thermal softening and shearing during sliding.

The oxide tribolayers on Ni-10Cr, Ni-20Cr and MA754 (**Figure 14**) exhibit extensive cracking parallel and perpendicular to the metal/oxide interface, and signs of buckling delamination due to compressive stresses during cooling at test shutdown. The channel cracks that develop in the tribolayer result from high contact loads, high thermal stresses, and incompatible deformation between the brittle oxide tribolayer and ductile underlying metal. The metal/oxide interfaces of

Ni-20Cr and MA754 also feature large oxide nodules which likely result from breakaway oxidation caused by Cr depletion in the underlying metal [32–34]. The wavelength of the nodules roughly matches the spacing of periodic cracks on the rubbing surface. The effects of this corrugated interface on interfacial fracture toughness, oxide delamination, and frictional ignition resistance are discussed below.

5.2. Effects of Cr content

5.2.1. Oxide tribolayer on commercial purity Ni

The Ni tribolayer and underlying metal are shown in **Figure 15a**. The tribolayer comprises a 13 µm thick layer of single-phase NiO, with equiaxed micron-scale grains near the free surface and nanograins with high porosity near the metal/oxide interface. In the underlying metal, there is porosity near the metal/oxide interface as well as a 20 µm thick layer of recrystallized micron-scale grains. There is no microstructural evidence of melting in either the tribolayer or base metal, consistent with the peak interfacial temperature of 1380 K, which is well below the melting points of Ni (1710 K) and NiO (2230 K). Based on the tribolayer thickness and the thermal conductivity of NiO we estimate a temperature drop of only 2 K across the tribolayer during testing.

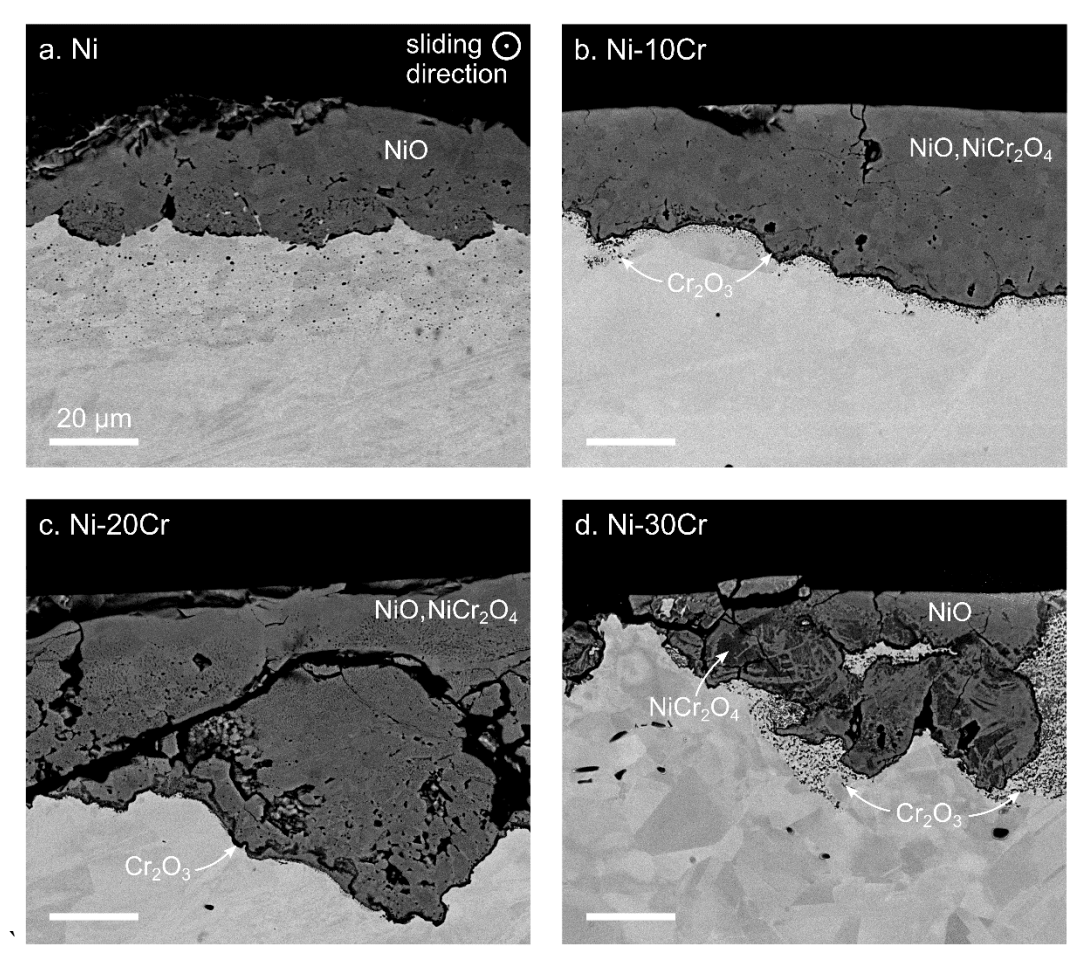


Figure 15: SEM micrographs of tribolayers formed during frictional ignition testing of non-ODS Ni-Cr alloys – (a) Ni, (b) Ni-20Cr, (c) Ni-20Cr, (d) Ni-30Cr. Images are high-magnification views of boxed regions in **Figure 14**.

Comparing the tribolayer in **Figure 15a** with oxide overlayers grown under static conditions suggests oxidation is much faster during high-speed sliding. A 10 µm thick NiO scale takes longer than 10 minutes to grow during static oxidation at 1273 K [35,36], whereas a similarly thick overlayer forms in 1 minute during frictional ignition testing. One possible explanation for the faster oxidation rates during frictional ignition is the high oxygen partial pressures. However, previous high-temperature Ni oxidation studies have shown that the oxidation rate is insensitive to oxygen pressure above 0.1 MPa [37]. The more likely explanation is that the fine grain structure in the oxide tribolayer enhances oxidation kinetics by enabling short-circuit diffusion of Ni ions along grain boundaries [38–40].

The fine grain structure in the NiO tribolayer (**Figure 15a**) likely arises from a combination of effects. First, the extent of grain growth is limited by the short test duration and by chemical impurities, which drag oxide grain boundaries. In addition, the tribolayer may inherent the fine grain structure of the underlying metal. Such behavior has been observed in static oxidation experiments which showed that NiO overlayers grown on coldworked Ni had finer grains than oxide scales grown on annealed samples [39,41–44].

Ni exhibits poor frictional ignition resistance despite having a high thermal effusivity because of its high friction coefficient, which results in a high frictional heating rate (see **Figure 12**). Based on the present microstructural observations, we hypothesize that its high friction coefficient stems from the low yield strength of Ni and the thin, porous tribolayer. During sliding, the underlying metal thermally softens and deforms, rupturing the thin NiO tribolayer, exposing soft Ni, and promoting the formation of metallurgical junctions that increase the friction coefficient.

5.2.2. Oxide tribolayers on Ni-Cr alloys

Figure 16 presents an XRD pattern collected from the Ni-20Cr tribolayer, revealing a mixture of two phases – NiO and NiCr₂O₄. XRD patterns from the tribolayers on the other Ni-Cr alloys were similar.

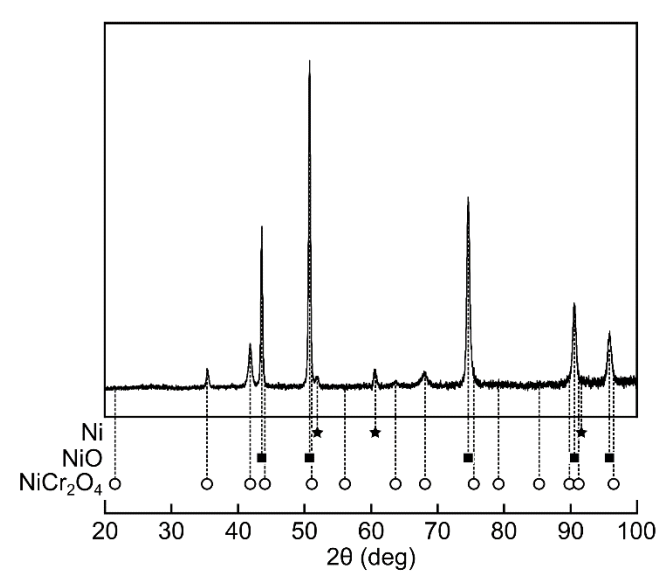


Figure 16: XRD pattern from the tribolayer on a non-ignited Ni-20Cr sample. Data was collected using a Co X-ray source.

Figures 15b–d show the oxide tribolayers on Ni-10Cr, Ni-20Cr, and Ni-30Cr. EDS maps of the oxide tribolayers agree with XRD results, revealing a dense upper layer of NiO at the gas/oxide interface, a middle layer of NiO with sub-micron NiCr₂O₄ precipitates (mean size ~500 nm), followed by a 1–5 μm thick Cr₂O₃ layer at the metal/oxide interface. The Ni-10Cr and Ni-30Cr tribolayers also feature a region of internal oxidation near the metal/oxide interface. NiCr₂O₄ islands form during the early stages of static oxidation of Ni-Cr alloys via a solid-state reaction between NiO and Cr₂O₃. During extended oxidation experiments these islands typically join into a thin continuous interlayer below the NiO outer layer [45,46]. This NiCr₂O₄ interlayer is absent from the tribolayer because the spinel precipitates do not have time to coalesce during the brief frictional ignition experiments. The Cr₂O₃ interlayer at the metal/oxide interface appears in static oxidation experiments of Ni-Cr alloys with more than 10 wt% Cr [46–49]. This phase was absent from the XRD patterns because X-rays could not penetrate the thick Ni-rich layers near the free surface. In all non-ODS Ni-Cr alloys, we observed porosity in the middle NiCr₂O₄/NiO layer, with larger pores closer to the Cr₂O₃ interlayer.

Figure 17 shows an O₂ pressure-temperature predominance diagram for Ni-20Cr. This diagram indicates that NiO and NiCr₂O₄ form closer to the oxide/gas interface, followed by a layer of metallic Ni and NiCr₂O₄, then a mixture of Cr₂O₃ and metallic Ni at the metal/oxide interface. We do not observe metallic Ni in the NiO/NiCr₂O₄ and Cr₂O₃ layers in **Figure 15** because they were too small to be resolved with SEM. There is generally good agreement between the predominance diagram and the observed oxide structures, suggesting equilibrium calculations can describe the phases within oxide tribolayers.

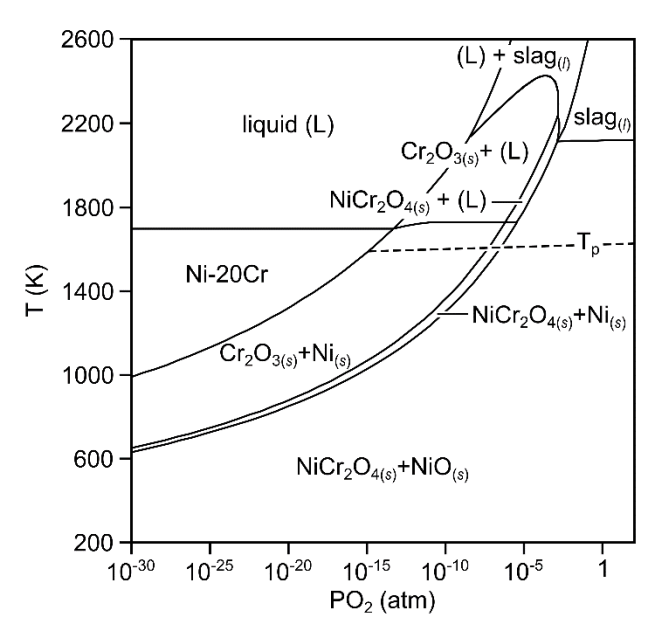


Figure 17: Predominance diagram for Ni-20Cr. The broken line indicates the expected temperature drop across the oxide tribolayer at ignition.

Similar to Ni, the non-ODS Ni-Cr alloys exhibit faster oxidation kinetics during high-speed sliding compared to static oxidation. Under static oxidation conditions (T = 1473 K, $PO_2 = 101 \text{ kPa}$), Ni-20Cr grows an 8 µm thick oxide over an exposure time of ~72 hours [48]. The Ni-20Cr

tribolayer formed during frictional ignition experiments reached an average thickness of 52 μm in 117 s at similar temperatures. The high PO₂ in the present study may have an effect on oxidation kinetics but it is unlikely to explain this dramatic difference in oxide thickness given the brief test duration. We hypothesize that the faster oxidation rates are in part due to the small NiCr₂O₄ particles in the NiO scale, which increase the mobility of Ni ions through the tribolayer by increasing the cation vacancy concentration [47–50]. In addition, NiCr₂O₄ particles pin NiO grain boundaries, resulting in a fine grain structure in the NiO layer that enables short-circuit diffusion of the Ni ions through grain boundaries [40,50,51]. Channel cracks in the tribolayer may facilitate O₂ ingress as well.

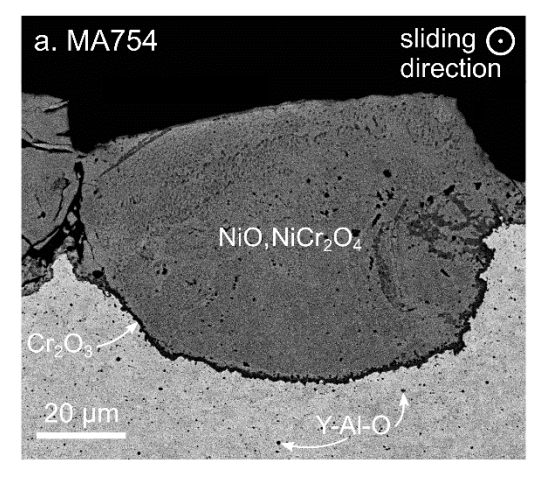
Despite the difference in oxidation kinetics, the microstructures of the Ni-10Cr and Ni-20Cr tribolayers are qualitatively similar to the structure of oxides grown on these alloys under static oxidation conditions (T = 1073-1473 K, $PO_2 = 101$ kPa) [46,48,49,52]. The close resemblance suggests that for these compositions, the dominant oxidation mechanisms under high-speed sliding and static oxidation are similar. This parallel breaks down at high Cr concentrations, as the Ni-30Cr tribolayer differs strongly from the oxide overlayer grown on Ni-30Cr during static oxidation. Internal oxidation like that seen in the Ni-30Cr tribolayer is typically absent from oxide overlayers formed on Ni-30Cr alloys (T = 1423 K, $PO_2 = 0.1$ kPa) [32]. Instead, the Ni-30Cr oxide tribolayer resembles oxide scales formed during static oxidation of low-Cr alloys (T = 1423 K, T = 1423

A key feature of the Ni-20Cr tribolayer is the wavy metal/oxide interface since this increases the interfacial fracture toughness of the tribolayer. Sehr et al. [53] have modeled the energy release rates required to drive cracks through wavy interfaces. Following their analysis, the interfacial toughening increment depends on the interface geometry (amplitude A and wavelength λ of the corrugations) and the ratio of bulk oxide toughness to interface toughness, G_b/G_i. From stereological measurements of the wavy interface on the Ni-20Cr tribolayer, we calculated a mean aspect ratio A/ λ of 0.2. Using reported toughness values of bulk NiO and Cr₂O₃ (10–15 J/m² [54,55]) and interfacial toughness values of NiO, Cr₂O₃, Al₂O₃ on Ni-based alloys (~10– 200 J/m² [56,57]), we estimate a G_b/G_i of 0.1–1.2. Based on our G_b/G_i , A/λ , and the results from Sehr et al. [53], we expect a 30% increment in the toughness at the crests and troughs of the wavy interface and a 60% increment near the rising and falling regions. The higher increment near the rising and falling regions results from an increase in mode-mixity as the crack propagates through the interface. At the crests and troughs, the mode-mix phase angle (ϕ) is 0° such that the crack propagates under pure mode I. As the crack moves away from these regions, φ increases to ~40° indicative of a mixed-mode behavior, which hinders the crack from propagating through the interface, causing it to kink into the oxide. Kinking of interfacial cracks from the metal/oxide interface into the bulk oxide is clearly visible in the Ni-20Cr tribolayer (Figure 14c). This preferred kinking behavior combined with a higher effective interface toughness prevents the oxide tribolayer from delamination along the metal/oxide interface.

Comparing the flat thin tribolayer on Ni with the thicker corrugated tribolayers on the non-ODS Ni-Cr alloys reveals distinct microstructural features that enhance frictional ignition resistance. In particular, the continuous Cr₂O₃ interlayer and corrugated metal/oxide interface in the Ni-10Cr and Ni-20Cr alloys improve tribolayer adhesion and interfacial toughness, mitigating tribolayer breakdown, lowering the friction coefficient, and increasing the ignition temperature. Among the non-ODS Ni-Cr alloys, Ni-20Cr was the most ignition-resistant because it grew the thickest oxide and had the most corrugated interface – the oxide nodules in Ni-20Cr are 120–140 µm thick while those in Ni-10Cr are only 60–100 µm thick.

5.3. Effects of Y_2O_3 dispersoids

Figure 18 compares high-magnification SEM micrographs of the oxide tribolayers on MA754 and MA758. The MA754 tribolayer has an average thickness of 80 μm, which is substantially thicker than the Ni-20Cr tribolayer (50 µm), despite running for the same time and achieving similar interfacial temperatures. In contrast, the mean thickness of the MA758 tribolayer is only 30 μm, which is thinner than that of Ni-30Cr (45 μm). The MA754 and MA758 tribolayers comprise multiple layers – a 10–20 µm thick layer of NiO closest to the rubbing surface, a 20–60 μm thick middle layer consisting of a NiO matrix with NiCr₂O₄ precipitates, and a 1 μm thick continuous Cr₂O₃ layer at the metal/oxide interface. Both tribolayers feature a gradient in grain size, with small equiaxed grains (~500 nm) near the Cr₂O₃/Ni-rich oxide interface and larger micron-scale grains at the oxide/gas interface. The tribolayers also have a corrugated metal/oxide interface, similar to that observed in Ni-20Cr. The tribolayers contain pores and crack-like defects at the metal/oxide interface due to incompatible plastic deformation. In MA754, the metal adjacent to the tribolayer has an equiaxed, recrystallized grain structure, with a mean grain size of ~1 μm. This is orders of magnitude smaller than the initial average grain size of several hundred microns. The fine grain size results from a combination of dynamic recrystallization during plastic deformation and Zener pinning by the oxide dispersoids. The MA758 feedstock had a fine grain structure at the start of the test, which was preserved during sliding.



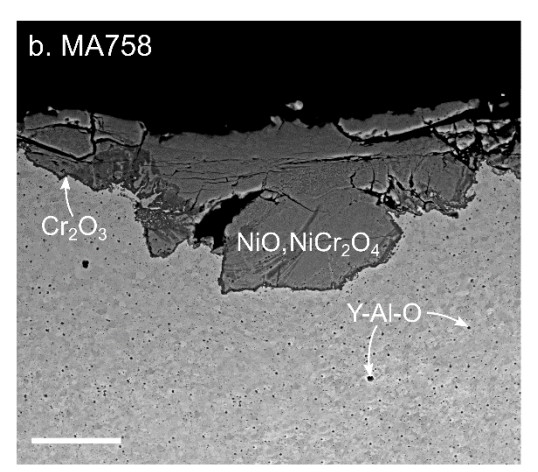


Figure 18: SEM micrographs of tribolayers formed during frictional ignition testing of ODS Ni-Cr alloys – (a) MA754, (b) MA758. Images are high-magnification views of boxed regions in **Figure 14**.

Similar to their non-ODS counterparts, ODS Ni-Cr alloys oxidize more rapidly during frictional ignition tests than under static oxidation conditions. Comparing the non-ODS and ODS tribolayers shows that the effect of Y_2O_3 on oxidation rate varies with Cr content. The MA758 tribolayer is thinner than that of Ni-30Cr, suggesting Y_2O_3 slows oxidation. Conversely, MA754 forms a much thicker oxide than Ni-20Cr $-80~\mu m$ v. $50~\mu m$ - despite similar test durations.

Figure 19 presents a STEM high-angle annular dark-field (HAADF) micrograph of the metal/oxide interface in MA754 and STEM EDS maps of a select region. The Cr₂O₃ interlayer has a fine grain structure with 250–500 nm grains, appreciably smaller than the grains in the underlying metal or in the Ni-rich oxide layer. This fine grain structure results from Zener pinning by metallic Ni particles seen in the EDS maps. Pores (0.5–1 μm in diameter) are observed at the interface between the Cr₂O₃ interlayer and the Ni-rich oxide. Y in the Cr₂O₃ interlayer is sequestered in Y-Al oxide particles that peg the oxide tribolayer, improving metal/oxide adhesion. **Figure 20** shows an EDS linescan across a NiO grain boundary (magenta arrow in **Figure 19**), revealing Y grain boundary segregation which may retard grain growth via solute drag.

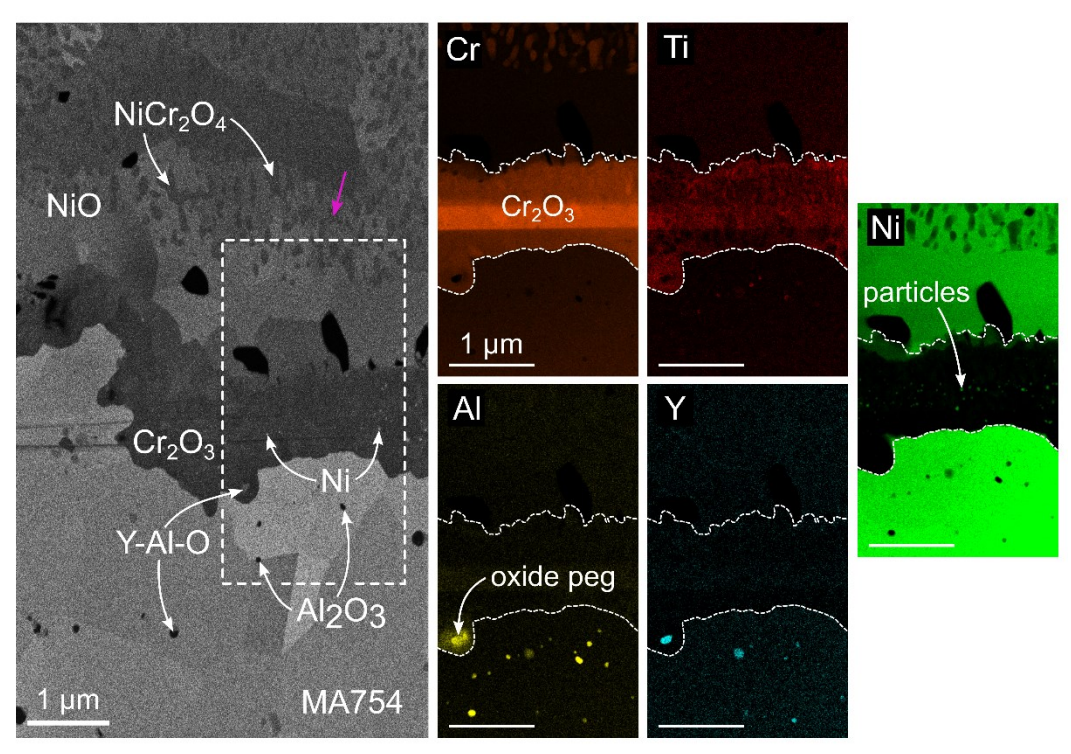


Figure 19: STEM micrograph and EDS mapping of the metal/oxide interface in the tribolayer of MA754. Magenta arrow indicates location and direction of the EDS linescan across a grain boundary shown in **Figure 20**. EDS elemental composition maps of the highlighted area are shown on the right.

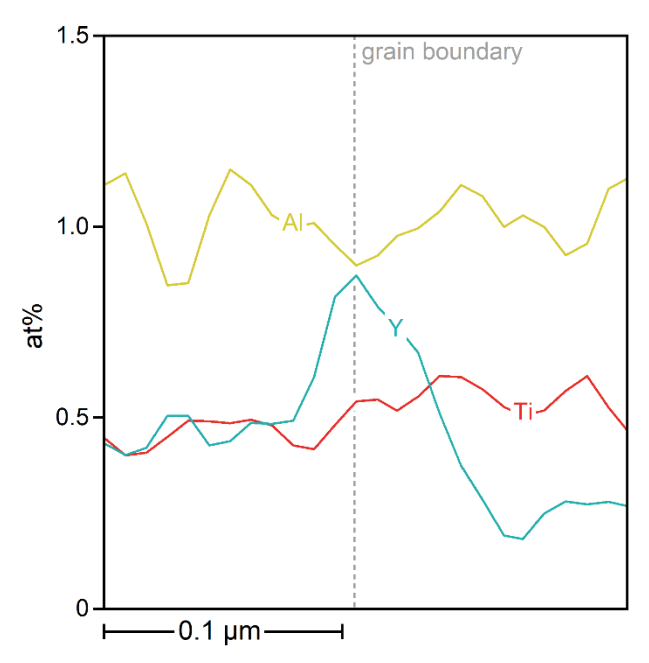


Figure 20: EDS linescan across a grain boundary. Location and direction of linescan correspond to the magenta arrow in **Figure 19**.

The Cr EDS map in **Figure 19** reveals Cr depletion within \sim 1 µm of the metal/oxide interface, confirming that the large oxide nodules form via breakaway oxidation. Further evidence of breakaway oxidation is the large NiCr₂O₄ islands in the NiO matrix shown in **Figure 21**. These islands were part of a continuous Cr₂O₃ layer prior to breakaway oxidation. Once the growth instability occurred, the Cr₂O₃ reacted with NiO to form the NiCr₂O₄ islands. As discussed above, the wavy interface generated by this growth instability increases interfacial fracture toughness helping to suppress oxide breakdown.

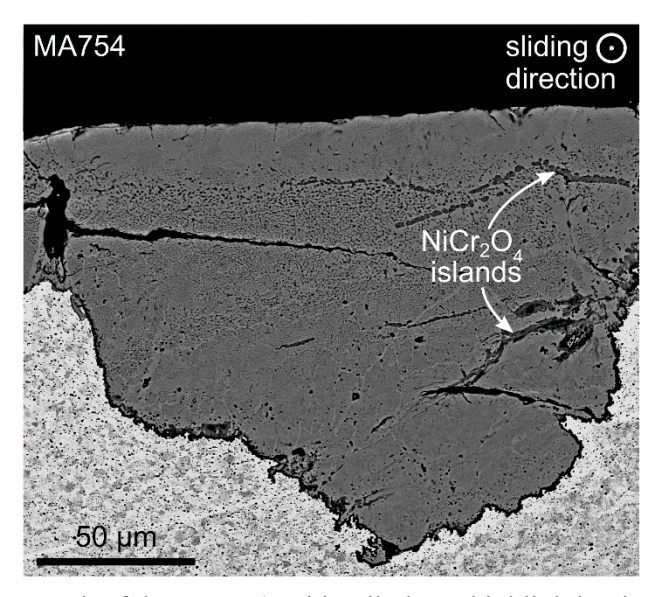


Figure 21: SEM micrograph of the MA754 oxide tribolayer highlighting large NiCr₂O₄ islands in the NiO matrix that likely were part of a continuous Cr₂O₃ layer prior to breakaway oxidation.

In **Figure 19**, the oxide particles in the underlying metal are mostly Y-Al mixed oxides $(Y_3Al_5O_{12}, YAlO_3, Y_4Al_2O_9)$ which form via reactions between Y_2O_3 dispersoids and Al. These oxide particles are much larger than the initial dispersoid size of ~20 nm presumably because their low melting points result in a high solubility in the Ni-matrix, which promotes coarsening. While coarsening of the Y-Al dispersoids degrades high-temperature mechanical properties, the present results indicate that it does not affect ignition resistance. This conclusion suggests that dispersoid chemistry may have a weak effect on frictional ignition resistance.

Comparing the tribolayers on the Ni-20Cr/MA754 pair reveals distinct microstructural features resulting from Y₂O₃ addition that enhance frictional ignition resistance. Oxide pegs in the Cr₂O₃ interlayer in MA754 improve metal/oxide adhesion. Y₂O₃ also refines the grain structure in the underlying metal, which in turn promotes a fine grain structure in the oxide tribolayer [39,40]. Grain size refinement of the oxide accelerates tribolayer growth through short-circuit diffusion. Considered together, faster oxidation kinetics enable MA754 to grow a thick tribolayer while an adherent metal/oxide interface mitigates tribolayer breakdown, lowering the friction coefficient and increasing the ignition temperature.

In the Ni-30Cr/MA758 pair, Y₂O₃ addition had only a minor impact on ignition resistance. The lack of a synergistic effect between Y₂O₃ and 30 wt% Cr is likely due to slower oxidation kinetics observed in Ni-30Cr v. Ni-20Cr [32,50]. Under high-temperature static conditions, Ni-30Cr quickly forms a continuous Cr₂O₃ interlayer, resulting in slower oxidation kinetics and a thinner oxide than Ni-20Cr. This effect is also observed in the present frictional ignition experiments when comparing the Ni-20Cr and Ni-30Cr tribolayers (**Figures 14c** and **14e**). Close inspection of the MA748 tribolayer suggests that Y₂O₃ addition further slows tribolayer growth (**Figures 14e** and **14f**). As noted above, this behavior contrasts with that of MA754, where Y₂O₃ accelerates tribolayer growth, but is consistent with conventional static oxidation results, where Y₂O₃ catalyzes formation of a slow-diffusing Cr₂O₃ interlayer [6–9] and blocks short-circuit diffusion by segregating to oxide grain boundaries [58,59]. Thus, while Y₂O₃ imparts MA758 with high-temperature strength, the thin MA758 tribolayer is susceptible to breakdown, resulting in a marginal increase in ignition resistance from Y₂O₃ addition.

6. Alloying effects on tribolayer mechanical properties

Figure 22 shows the nanoindentation hardness of the oxide and underlying metal near the metal/oxide interface as a function of Cr content. The hardness values of the underlying metal and oxide are consistent with literature data for Ni-Cr alloys [60] and oxide ceramics [61,62]. Comparing the hardness of the non-ODS alloys shows that Cr addition increases the room-temperature hardness of the underlying metal through solid solution strengthening. Cr addition also increases the oxide hardness via formation of NiCr₂O₄ precipitates within the NiO matrix, in concentrations ranging from 13 vol% for Ni-10Cr to 42 vol% for Ni-30Cr. While the oxide tribolayer will thermally soften [63], we expect that the trend of increasing oxide hardness with Cr content will persist to high temperatures because the strength of Ni₂CrO₄ is less temperature-sensitive than that of NiO [64]. The increase in hardness with Cr addition reduces the likelihood of junction growth during sliding, resulting in a lower friction coefficient, consistent with the trend in **Figure 6**.

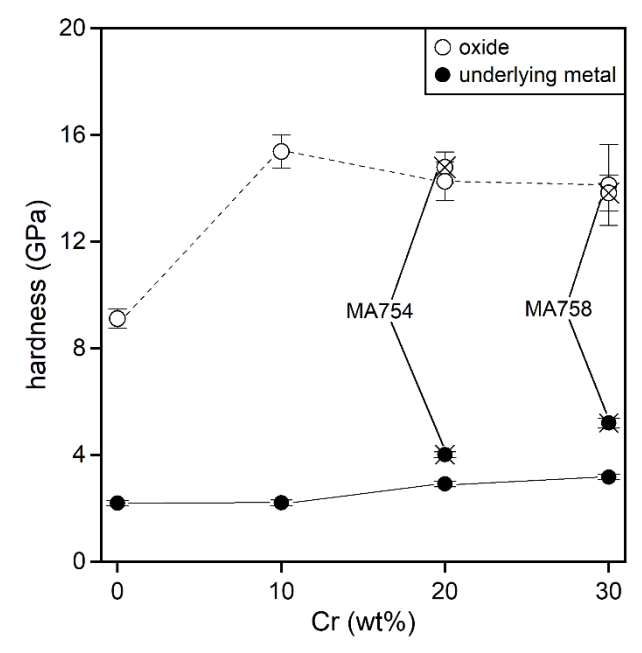


Figure 22: Hardness of the oxide and underlying metal near the metal/oxide interface as a function of Cr content. These specimens were tested under: $PO_2 = 6.9 \text{ MPa}$, v = 22 m/s, L = 31 N/s.

Comparing the hardness of the ODS alloys with their non-ODS counterparts, we observe that Y_2O_3 addition has minimal effect on oxide hardness. However, Y_2O_3 addition appreciably strengthens the underlying metal, making the underlying metal more resistant to plastic deformation and providing greater support to the tribolayer – effects which mitigate oxide breakdown.

7. Alloying effects on tribolayer stability

Cr addition enhances the ignition resistance of non-ODS Ni-Cr alloys by: (i) improving oxide tribolayer adhesion through the growth of a continuous, adherent Cr₂O₃ interlayer; (ii) increasing interfacial toughness through the formation of corrugated metal/oxide interface; and (iii) reducing the extent of plastic deformation during sliding by strengthening the underlying metal and the oxide tribolayer. While increasing Cr content helps mitigate tribolayer breakdown by strengthening the oxide and underlying metal, it also slows down oxidation kinetics by promoting the formation of the slow-diffusing Cr₂O₃ interlayer [32,45–47], which results in a thinner tribolayer that is more susceptible to breakdown. Ni-20Cr has an optimal Cr content that balances these competing effects, achieving a tribolayer structure that optimizes tribolayer growth and resistance to tribolayer breakdown and frictional ignition.

Addition of Y₂O₃ dispersoids can further improve ignition resistance, as demonstrated in the Ni-20Cr/MA754 material pair. The oxide dispersoids accelerate growth of the oxide tribolayer by refining the grain structure in the underlying metal via Zener pinning. This in turn promotes formation of a fine-grained oxide tribolayer that increases oxidation kinetics via short-circuit diffusion. The dispersoids also improve oxide adhesion by pegging the Cr₂O₃ interlayer, which increases the interfacial fracture toughness. Finally, the dispersoids strengthen the underlying metal, lessening the extent of plastic deformation. In the case of MA754, this combination of

faster oxidation kinetics, a more adherent oxide tribolayer, and less plastic deformation of the underlying metal augments the beneficial effects of Cr.

The material index presented in **Section 4** shows that ignition-resistant alloys should have a high thermal effusivity, low friction coefficient, and high ignition temperature. Optimizing friction coefficient and ignition temperature requires quickly forming an adherent, strong, and dense oxide tribolayer; toughening the metal/oxide interface, e.g., via corrugations in the oxidation front; and resisting plastic deformation at high temperatures. While these behaviors are all observed in MA754, similar results may be achieved in other dispersion-strengthened alloys. The STEM analysis indicates that the formation of mixed Y-Al oxides does not degrade ignition resistance, suggesting other dispersoid chemistries may be equally effective at enhancing frictional ignition resistance.

8. Conclusions

High-speed sliding experiments in high-pressure gaseous O₂ were used to assess the frictional ignition behaviors of binary Ni-Cr alloys and two ODS alloys (MA754, MA758). *In situ* measurements of friction coefficient and axial displacement were used along with calculations of the interfacial temperature at the rubbing surface to understand the effects of Cr additions and Y₂O₃ dispersoids on the mechanisms of tribolayer growth and frictional ignition. Complementary structural characterization of the rubbing surfaces of non-ignited recovered samples revealed the role of material chemistry on the composition, morphology, and spatial distribution of oxide phases within the tribolayer.

The key results of this study are as follows:

- All materials exhibited a decay in friction coefficient with time due to the *in situ* growth of a lubricating oxide tribolayer. The friction coefficient increased prior to ignition due to oxide tribolayer breakdown, exposing the hot underlying metal to high pressure O₂ and triggering ignition.
- Comparing the ignition behaviors of the non-ODS alloys with their ODS counterparts reveals that Y₂O₃ additions decrease the friction coefficient and the extent of plastic deformation. MA754 is the only material that did not ignite in any test. These results point towards a synergistic interplay between 20 wt% Cr content and Y₂O₃ dispersoids in MA754.
- The microstructure of the oxide tribolayers varied strongly with Cr content in the binary Ni-Cr alloys. All Ni-Cr alloys except Ni-30Cr developed a continuous 1 µm thick Cr₂O₃ interlayer at the metal/oxide interface. Above the Cr₂O₃ interlayer, there was a thicker overlayer that comprised a mixture of NiO and nanoscale NiCr₂O₄ precipitates.
- Ni-20Cr was the most ignition-resistant of the binary Ni-Cr alloys, with the lowest friction coefficient, highest ignition temperature, and longest ignition time. The unique behavior of Ni-20Cr is linked to key features of its tribolayer. Rapid oxidation kinetics result in a thick protective oxide with an adherent Cr₂O₃ interlayer. Large amplitude oscillations of the metal/oxide interface prevent metal exposure under oxide

- delamination. NiCr₂O₄ precipitates in the NiO matrix strengthen the oxide tribolayer, lowering the friction coefficient.
- The oxide tribolayer on MA754 exhibited many of the same features as the Ni-20Cr tribolayer. However, the Y₂O₃ addition affected the tribolayer chemistry and the microstructure underneath the tribolayer. Coarse Y-Al oxide dispersoids in the underlying metal pinned grain boundaries in the metal underneath the tribolayer, resulting in a fine recrystallized region. This grain structure promotes the growth of a fine-grained oxide tribolayer that accelerates tribolayer growth through short circuit diffusion. The more rapid oxidation in MA754 v. Ni-20Cr results in a thicker oxide tribolayer at a fixed time.
- Comparing the MA754 and Ni-20Cr tribolayers indicates that the addition of Y₂O₃ accelerates growth of the protective tribolayer, enhances interfacial toughness through dispersoid pegging, and mitigates plastic deformation of the underlying metal through dispersion-strengthening. These features collectively lower the friction coefficient, increase the ignition temperature, and suppress frictional ignition.

CRediT authorship contribution statement

Andres Garcia Jimenez: Conceptualization, Methodology, Investigation, Writing - Original Draft. Timothy Wabel: Methodology, Investigation. Fabio Bendana: Methodology, Investigation, Resources. John DeSain: Methodology, Investigation. Michael Xu: Methodology, Investigation. James LeBeau: Methodology, Supervision. Zachary Cordero: Conceptualization, Methodology, Writing - Review & Editing, Supervision.

Acknowledgments

This research was enabled by financial support from the NSF through grants DMR-2004913 and CMMI–1922206. A.G.J. gratefully acknowledges support from the NSF Graduate Research Fellowship Program through grant No. 2141064. We thank Dr. Yanice Benitez, Dr. Levon Gevorkyan, Armando Perezselsky, Dr. Vincent Phong, and Devon Smith from Aerospace Corporation for their support with the frictional ignition tests. Financial support for the experimental activities at Aerospace Corporation was provided by John di Pol and Dr. James Morehart. STEM sample preparation and characterization utilized Harvard University's Center for Nanoscale Systems (CNS) and the MIT.nano Characterization Facilities.

References

- [1] Benz FJ, Stoltzfus JM. Ignition of Metals and Alloys in Gaseous Oxygen by Frictional Heating. Flammability and Sensitivity of Materials in Oxygen-Enriched Atmospheres: Second Volume, vol. 2, ASTM International; 1999, p. 38–58. https://doi.org/10.1520/STP19308S.
- [2] Stoltzfus JM, Benz FJ, Homa J. The Pv product required for the frictional ignition of alloys. vol. 4, Las Cruces, NM: ASTM International; 1989, p. 212–27.
- [3] Homa J, Stoltzfus JM. The measurement of the friction coefficient and wear of metals in high-pressure oxygen. vol. 6, ASTM International; 1993, p. 389–403.

- [5] Schoenman L, Stoltzfus JM, Kazaroff J. Friction-induced ignition of metals in high-pressure oxygen. vol. 3, ASTM International; 1988, p. 105–33.
- [6] Stringer J, Wilcox BA, Jaffee RI. The high-temperature oxidation of nickel-20 wt. % chromium alloys containing dispersed oxide phases. Oxid Met 1972;5:11–47. https://doi.org/10.1007/BF00614617.
- [7] Wright IG, Wilcox BA, Jaffee RI. The high-temperature oxidation of Ni-20%Cr alloys containing various oxide dispersions. Oxid Met 1975;9:275–305. https://doi.org/10.1007/BF00613277.
- [8] Hou PY, Stringer J. The effect of reactive element additions on the selective oxidation, growth and adhesion of chromia scales. Materials Science and Engineering: A 1995;202:1–10. https://doi.org/10.1016/0921-5093(95)09798-8.
- [9] Pieraggi B, Rapp RA. Chromia Scale Growth in Alloy Oxidation and the Reactive Element Effect. J Electrochem Soc 1993;140:2844. https://doi.org/10.1149/1.2220920.
- [10] Kvernes IA. The role of yttrium in high-temperature oxidation behavior of Ni-Cr-Al alloys. Oxid Met 1973;6:45–64. https://doi.org/10.1007/BF00612046.
- [11] Pryzybylski K. High-temperature oxidation properties of ODS MA754 alloy. In: Embury JD, editor. High-Temperature Oxidation and Sulphidation Processes, Oxford: Pergamon; 1990, p. 346. https://doi.org/10.1016/B978-0-08-040423-3.50030-6.
- [12] Gevorkyan L, McCall S, Smolke J, Driscoll R. A Test Apparatus for the Characterization of Ignitability and Flammability of Metals in High Pressure Oxygen. AIAA Propulsion and Energy 2019 Forum, Indianapolis, IN: American Institute of Aeronautics and Astronautics; 2019. https://doi.org/10.2514/6.2019-4351.
- [13] Wabel TM, Bendana F, DeSain J, Gevorkyan L. Friction Ignition Testing of Metals in Oxygen up to 24.1 MPa, American Institute of Aeronautics and Astronautics; 2023, p. 1491. https://doi.org/10.2514/6.2023-1491.
- [14] Standard Guide for Cleanliness Levels and Cleaning Methods for Materials and Equipment Used in Oxygen-Enriched Environments 2019.
- [15] COMSOL Multiphysics® v. 6.2. www.comsol.com. COMSOL AB, Stockholm, Sweden.
- [16] Garcia Jimenez A, Cordero ZC. Frictional Ignition of Metals in High Pressure Oxygen: A Critical Reassessment of NASA Test Data, American Institute of Aeronautics and Astronautics; 2023, p. 1489. https://doi.org/10.2514/6.2023-1489.
- [17] Special Metals. Ni200 Product handbook of high performing nickel alloys. 2023.
- [18] Special Metals. Nimonic 75 Product handbook of high performing nickel alloys. 2023.
- [19] Special Metals. MA754 Product handbook of high performing nickel alloys. 2023.
- [20] Air Products and Chemicals Inc. Thermodynamic data on oxygen and nitrogen. Wright-Patterson Air Force Base OH: 1961.
- [21] Bale CW, Belisle E, Chartrand P, Decterov SA, Eriksson G, Gheribi AE, et al. FactSage Thermochemical Software and Databases 2010.
- [22] Earles SWE, Kadhim MJ. Friction and Wear of Unlubricated Steel Surfaces at Speeds up to 655 FT/S. Proceedings of the Institution of Mechanical Engineers 1965;180:531–48. https://doi.org/10.1243/PIME_PROC_1965_180_037_02.
- [23] Cocks M. Role of Atmospheric Oxidation in High Speed Sliding Phenomena-I. Journal of Applied Physics 1957;28:835–43. https://doi.org/10.1063/1.1722871.
- [24] Cocks M. The Role of Atmospheric Oxidation in High Speed Sliding Phenomena—II. ASLE Transactions 1958;1:101–7. https://doi.org/10.1080/05698195808972320.

- [25] Stott FH, Lin DS, Wood GC, Stevenson CW. The tribological behaviour of nickel and nickel-chromium alloys at temperatures from 20° to 800 °C. Wear 1976;36:147–74. https://doi.org/10.1016/0043-1648(76)90002-8.
- [26] Stott FH, Wood GC. The influence of oxides on the friction and wear of alloys. Tribology International 1978;11:211–8. https://doi.org/10.1016/0301-679X(78)90178-0.
- [27] Powell DG, Earles SWE. Wear of Unlubricated Steel Surfaces in Sliding Contact. ASLE Transactions 1968;11:101–8. https://doi.org/10.1080/05698196808972213.
- [28] Lim SC, Ashby MF. Overview no. 55 Wear-Mechanism maps. Acta Metallurgica 1987;35:1–24. https://doi.org/10.1016/0001-6160(87)90209-4.
- [29] Korkmaz ME, Günay M. Confirmation of Johnson-Cook Model Parameters for Nimonic 80A alloy by Finite Element Method. Politeknik Dergisi 2020;23:625–32. https://doi.org/10.2339/politeknik.555271.
- [30] McIlroy K, Zawierucha R, Drnevich RF. Promoted Ignition Behavior of Engineering Alloys in High-Pressure Oxygen. vol. 3, ASTM International; 1988, p. 85–104. https://doi.org/10.1520/STP26741S.
- [31] Million JF, Samant AV, Zawierucha R. Promoted Ignition-Combustion Behavior of Tubular Aluminum Samples in Liquid and Gaseous Oxygen Environments. vol. 10, ASTM International; 2003, p. 192–208. https://doi.org/10.1520/STP11589S.
- [32] Wood GC, Stott FH. Oxidation of alloys. Materials Science and Technology 1987;3:519–30. https://doi.org/10.1080/02670836.1987.11782263.
- [33] Evans HE, Donaldson AT, Gilmour TC. Mechanisms of Breakaway Oxidation and Application to a Chromia-Forming Steel. Oxidation of Metals 1999;52:379–402. https://doi.org/10.1023/A:1018855914737.
- [34] Gong Y, Young DJ, Kontis P, Chiu YL, Larsson H, Shin A, et al. On the breakaway oxidation of Fe9Cr1Mo steel in high pressure CO2. Acta Materialia 2017;130:361–74. https://doi.org/10.1016/j.actamat.2017.02.034.
- [35] Peraldi R, Monceau D, Pieraggi B. Correlations Between Growth Kinetics and Microstructure for Scales Formed by High-Temperature Oxidation of Pure Nickel. II. Growth Kinetics. Oxidation of Metals 2002;58:275–95. https://doi.org/10.1023/A:1020102604090.
- [36] Peraldi R, Monceau D, Pieraggi B. Correlations Between Growth Kinetics and Microstructure for Scales Formed by High-Temperature Oxidation of Pure Nickel. I. Morphologies and Microstructures. Oxidation of Metals 2002;58:249–73. https://doi.org/10.1023/A:1020170320020.
- [37] Baur JP, Bartlett RW, Ong JN, Fassell WM. High-Pressure Oxidation of Metals, Nickel in Oxygen. J Electrochem Soc 1963;110:185. https://doi.org/10.1149/1.2425708.
- [38] Atkinson A. Wagner theory and short circuit diffusion. Materials Science and Technology 1988;4:1046–51. https://doi.org/10.1179/mst.1988.4.12.1046.
- [39] Graham MJ, Caplan D, Hussey RJ. The Effect of Oxide Grain Structure on the High-Temperature Oxidation of Fe, Ni and Cr. Canadian Metallurgical Quarterly 1979;18:283–91. https://doi.org/10.1179/cmq.1979.18.3.283.
- [40] Atkinson HV. A review of the role of short-circuit diffusion in the oxidation of nickel, chromium, and nickel-chromium alloys. Oxid Met 1985;24:177–97. https://doi.org/10.1007/BF00664231.
- [41] Rigney DA. Sliding Wear of Metals. Annual Review of Materials Science 1988;18:141–63. https://doi.org/10.1146/annurev.ms.18.080188.001041.

- [42] Rigney DA, Hirth JP. Plastic deformation and sliding friction of metals. Wear 1979;53:345–70. https://doi.org/10.1016/0043-1648(79)90087-5.
- [43] Rigney DA, Fu XY, Hammerberg JE, Holian BL, Falk ML. Examples of structural evolution during sliding and shear of ductile materials. Scripta Materialia 2003;49:977–83. https://doi.org/10.1016/S1359-6462(03)00472-X.
- [44] Guo XK, Luo ZP, Li XY, Lu K. Plastic deformation induced extremely fine nano-grains in nickel. Materials Science and Engineering: A 2021;802:140664. https://doi.org/10.1016/j.msea.2020.140664.
- [45] Wood GC, Wright IG, Hodgkiess T, Whittle DP. A Comparison of the Oxidation of Fe&&bond; Cr, Ni-Cr and Co-Cr alloys in oxygen and water vapour. Materials and Corrosion 1970;21:900–10. https://doi.org/10.1002/maco.19700211105.
- [46] Wood GC, Hodgkiess T. Characteristic Scales on Pure Nickel-Chromium Alloys at 800°–1200°C. J Electrochem Soc 1966;113:319. https://doi.org/10.1149/1.2423955.
- [47] Wallwork GR. The oxidation of alloys. Rep Prog Phys 1976;39:401–85. https://doi.org/10.1088/0034-4885/39/5/001.
- [48] Zima GE. Some high temperature oxidation characteristics of nickel with chromium additions. PhD. California Institute of Technology, 1956. https://doi.org/10.7907/8MC2-WR66
- [49] Giggins CS, Pettit FS. Oxidation of Ni Cr Al Alloys Between 1000° and 1200°C. J Electrochem Soc 1971;118:1782. https://doi.org/10.1149/1.2407837.
- [50] Wood GC. High-temperature oxidation of alloys. Oxid Met 1970;2:11–57. https://doi.org/10.1007/BF00603581.
- [51] Xue F, Marquis EA. Role of diffusion-induced grain boundary migration in the oxidation response of a Ni-30 Cr alloy. Acta Materialia 2022;240:118343. https://doi.org/10.1016/j.actamat.2022.118343.
- [52] Giggins CS. The Effect of Alloy Grain-Size and Surface Deformation on the Selective Oxidation of Cr in Ni-Cr Alloys at Temperatures of 900 and 1100°C. Trans TMS-AIME 1969;245:2509–15.
- [53] Sehr S, Amidi S, Begley MR. Interface delamination vs. bulk cracking along wavy interfaces. Engineering Fracture Mechanics 2019;206:64–74. https://doi.org/10.1016/j.engfracmech.2018.10.031.
- [54] Tromans D, Meech JA. Fracture toughness and surface energies of minerals: theoretical estimates for oxides, sulphides, silicates and halides. Minerals Engineering 2002;15:1027–41. https://doi.org/10.1016/S0892-6875(02)00213-3.
- [55] Nose T, Fujii T. Evaluation of Fracture Toughness for Ceramic Materials by a Single-Edge-Precracked-Beam Method. Journal of the American Ceramic Society 1988;71:328–33. https://doi.org/10.1111/j.1151-2916.1988.tb05049.x.
- [56] Qi YH, Bruckel P, Lours P. Interfacial toughness of the nickel–nickel oxide system. Journal of Materials Science Letters 2003;22:371–4. https://doi.org/10.1023/A:1022697110703.
- [57] Zurek J, Young DJ, Essuman E, Hänsel M, Penkalla HJ, Niewolak L, et al. Growth and adherence of chromia based surface scales on Ni-base alloys in high- and low-pO2 gases. Materials Science and Engineering: A 2008;477:259–70. https://doi.org/10.1016/j.msea.2007.05.035.
- [58] Pint BA. Experimental observations in support of the dynamic-segregation theory to explain the reactive-element effect. Oxid Met 1996;45:1–37. https://doi.org/10.1007/BF01046818.

- [59] Alexander KB, Prusner K, Pint BA, Tortorelli PF. The effect of reactive-element alloying additions on the microstructure and microchemistry of thermally-grown oxide scales on nickel-based alloys. Energy 1998;12:16.
- [60] Bauer JRO, Loguercio AD, Reis A, Rodrigues Filho LE. Microhardness of Ni-Cr alloys under different casting conditions. Braz Oral Res 2006;20:40–6. https://doi.org/10.1590/S1806-83242006000100008.
- [61] Roy TK. Assessing hardness and fracture toughness in sintered zinc oxide ceramics through indentation technique. Materials Science and Engineering: A 2015;640:267–74. https://doi.org/10.1016/j.msea.2015.05.107.
- [62] Nicholls JR, Hall DJ, Tortorelli PF. Hardness and modulus measurements on oxide scales. Materials at High Temperatures 1994;12:141–50. https://doi.org/10.1080/09603409.1994.11689480.
- [63] Salari S, Rahman MS, Polycarpou AA, Beheshti A. Elevated temperature mechanical properties of Inconel 617 surface oxide using nanoindentation. Materials Science and Engineering: A 2020;788:139539. https://doi.org/10.1016/j.msea.2020.139539.
- [64] Frost HJ, Ashby MF. Deformation-mechanism maps: the plasticity and creep of metals and ceramics. Cambridge UK: Franklin Book Company; 1995.

Appendix 1. Material index for frictional ignition resistance

A material index is a grouping of material properties whose extremal value maximizes performance in a given application. An important advantage of using material indices in material selection is they are not limited to a specific set of test conditions. As an example, test data can be used to determine a material index for ignition resistance under one set of conditions, which is then easily generalized to other conditions without further experiments. To develop a material index for frictional ignition resistance, we first recognize that our objective is always to maximize the ignition time, t_s , regardless of the sliding conditions. Approximating the frictional ignition specimen as a 1D semi-infinite body with a constant heat flux boundary condition q, the time to a reach a given increment in interfacial temperature ΔT is

$$t = \left(\frac{1}{q}(\Delta T)\sqrt{\rho C_p \kappa}\right)^2,\tag{A1}$$

where $\sqrt{\rho C_p \kappa}$ is the thermal effusivity. The frictional heat flux q is given by

$$q = \alpha \mu P v, \tag{A2}$$

where α is the heat partition coefficient. Assuming the specimen has an initial uniform temperature T_0 and a material-specific ignition temperature T_{ign} , the temperature increment at ignition is

$$\Delta T = (T_{ign} - T_0). \tag{A3}$$

Combining Equations A1-A3 gives the objective function

$$t_{s} = \left(\frac{1}{\alpha P v}\right)^{2} \left[\frac{\left(T_{ign} - T_{0}\right)\sqrt{\rho C_{p} \kappa}}{\mu}\right]^{2}.$$
(A4)

Inspection of Equation A4 shows that we can maximize t_s by maximizing the material index

$$MI = \left[\frac{1}{\mu} \left(T_{ign} - T_0\right) \sqrt{\rho C_p \kappa}\right]^2. \tag{A5}$$

This is used in **Section 4** of the text to compare the intrinsic frictional ignition-resistance of different materials.